

Model Synthesis for Zero-Shot Model Attribution

Tianyun Yang, Juan Cao, Danding Wang, Chang Xu

Abstract—Nowadays, generative models are shaping various fields such as art, design, and human-computer interaction, yet accompanied by challenges related to copyright infringement and content management. In response, existing research seeks to identify the unique fingerprints on the images they generate, which can be leveraged to attribute the generated images to their source models. Existing methods, however, are constrained to identifying models within a static set included in the classifier training, failing to adapt to newly emerged unseen models dynamically. To bridge this gap, we aim to develop a generalized model fingerprint extractor capable of zero-shot attribution, effectively attributes unseen models without exposure during training. Central to our method is a model synthesis technique, which generates numerous synthetic models mimicking the fingerprint patterns of real-world generative models. The design of the synthesis technique is motivated by observations on how the basic generative model’s architecture building blocks and parameters influence fingerprint patterns, and it is validated through two designed metrics that examine synthetic models’ fidelity and diversity. Our experiments demonstrate that this fingerprint extractor, trained solely on synthetic models, achieves impressive zero-shot generalization on a wide range of real-world generative models, improving model identification and verification accuracy on unseen models by over 40% and 15%, respectively, compared to existing approaches.

Index Terms—Model Fingerprint, Model Attribution, Model Synthesis, Zero-Shot Adaptation

I. INTRODUCTION

IN recent years, advanced generative (vision) models have revolutionized various fields such as art creation, design, and human-computer interaction [1]–[4]. Despite their positive impact, these models have also given rise to new concerns, such as copyright infringement issues and content supervision. To address these concerns, model attribution, the process of identifying the source model of generated content, has gained increasing attention [5]–[10]. It helps deter unauthorized copying and distribution, enabling content creators and rights holders to prove ownership and take legal action against infringements. Furthermore, model attribution allows regulators to identify and act against entities using generative models for harmful, illegal, or unethical purposes.

Existing research seeks to identify the unique fingerprints on the images they generate, which can be leveraged to attribute a generated image to its source model. A commonly adopted model attribution paradigm frames the task as a multi-class classification problem [6], [8]–[10]. In this setup, images generated by a limited and static set of models are used to train a classifier, where each image is labeled with a unique model

Tianyun Yang, Juan Cao, and Danding Wang are with the Institute of Computing Technology, Chinese Academy of Sciences, Beijing, China. E-mail: {yangtianyun19z, caojuan, wangdanding}@ict.ac.cn

Chang Xu is with School of Computer Science, Faculty of Engineering, University of Sydney, Australia. E-mail: c.xu@sydney.edu.au

Code: <https://github.com/TianyunYoung/Model-Fingerprint>

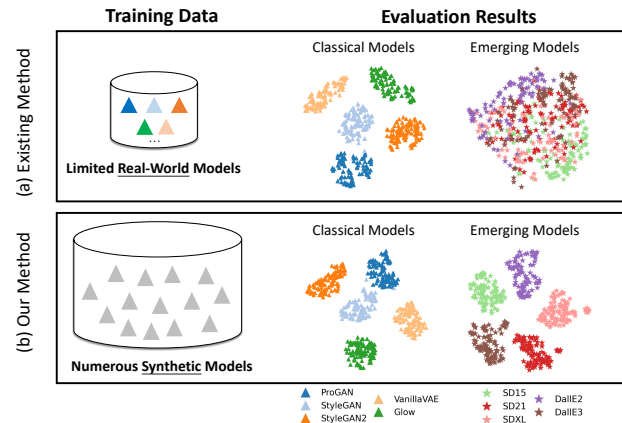


Fig. 1: Illustration of existing model attribution method (above) and our method (below). Existing methods rely on training with a limited set of real-world models, allows them to attribute seen classical models included in the training data. However, they struggle with generalizing to emerging unseen models like Stable Diffusion and DALL-E due to a gap in fingerprint distribution. Our method, in contrast, trains on numerous synthetic models that replicate a broader range of real-world generative model fingerprints, enabling it to attribute unseen models effectively in a zero-shot manner.

ID. During testing, the test image comes from a seen model predefined in the training set, and the classifier would identify the model ID of the image based on the model fingerprint it has learned [6], [8], [9]. However, there arises a scenario where a testing image originates from an unseen model not present during training. To tackle this, some methodologies [10], [11] adopt an open-set setup, assigning them an “unknown” label.

Despite these efforts, conventional methods, trained on a static set of seen models, struggle to adapt to the newly emerged unseen models dynamically. This limitation is exemplified in Figure 1(a), which presents the t-SNE feature extraction results from an existing method [10]. We train this method on classical models such as GAN, VAE, and Flow models¹, and test on both these and the emerging Diffusion models. The results reveal a significant generalization gap when the method encounters new types of generative models. This gap stems from the restricted scope of seen models that can be practically collected, whose fingerprint distributions may significantly differ from those of newly emerging models. As generative technology continues to evolve, the variety of unseen models expands, further challenging the capacity of existing methods to adapt dynamically.

To bridge this gap, our goal is to develop a more generalized

¹Include all the GAN, VAE, and Flow models in Table I

model fingerprint extractor capable of attributing unseen models efficiently in a zero-shot setting. Central to our approach is a model synthesis technique that creates plenty of synthetic models that mimic a broad range of fingerprint patterns in real-world generative models. To gain insights for replicating these patterns, our initial step is to explore why generative models display unique fingerprint patterns, which, although typically imperceptible in the spatial domain, manifest as distinct spectral patterns in high-frequency components. Through analyzing the architecture and parameters of generative models, we observe: 1) The type of basic network components such as upsampling, activation function, normalization, and parameters of convolution layers are key factors influencing the spectral patterns of the generated images. 2) Across the generative blocks within a large generative model, due to the upsampling layer that naturally attenuates earlier layers' high-frequency components, the last few generative blocks are more influential in determining the output's spectrum patterns.

We incorporate these observations into our model synthesis technique. Our approach is based on a shallow auto-encoder architecture, comprising fewer generative blocks compared to typical generative models. According to the discussion above, employing a synthesis architecture with a small number of generative blocks could ensure fidelity in mimicking fingerprints. We then increase the architecture diversity by varying the types of upsampling layers, activation functions, normalization layers, and the number and sequence of these layers. Additionally, we enhance the parameter diversity by altering training seeds. Consequently, this approach allows us to get 5760 synthetic models across 288 different architectures by minimizing the reconstruction loss. Owing to the simple architecture and training objective, training these synthetic models requires much less time than real generative models. Subsequently, we leverage these synthetic models to train the fingerprint extractor, to extract fingerprints from these models, and distinguish between each other. We combine classification and metric loss to enhance the discrimination of learned fingerprint embedding.

We establish two metrics to verify the effectiveness of our model synthesis strategy in terms of *fidelity* and *diversity*. The former assesses the authenticity of fingerprint pattern mimicking by comparing the spectrum distribution between synthetic and real models, particularly in high-frequency components. The latter evaluates the diversity of spectrum patterns of synthetic models by examining the extent to which the synthetic models occupy the spectrum representation space. The results indicate that the synthesis options we designed indeed enhance the distribution fidelity and diversity of spectrum patterns.

Experimental results demonstrate that our fingerprint extractor, despite being solely trained on synthetic models, exhibits strong zero-shot attribution capabilities on a broad scope generative models, including the classical GAN, VAE, Flow models, and emerging Diffusion models like Stable Diffusion and DalleE-3. Partial visualization results are shown in Figure 1(b). In the model attribution scenarios, including model identification and verification on unseen models, our method significantly outperforms existing approaches, achiev-

ing accuracy improvements of over 40% and 15% respectively.

Our major contributions can be summarized as follows:

1) We propose to address a practical problem in applying model attribution in the real world, to expand the attribution target to unseen models in a zero-shot setting.

2) We propose to solve the zero-shot model attribution problem based on training on numerous synthetic models, which mimic the fingerprint patterns of real-world generative models. The synthesis strategy is motivated by observations on how generative model architecture building blocks and parameters influence fingerprint patterns and is validated through two designed metrics that examine synthetic models' fidelity and diversity.

3) Experimental results demonstrate that our fingerprint extractor, trained on synthetic models, exhibits strong generalization capabilities on a wide range of real-world generative models. Compared with existing methods, we improve the model identification and verification accuracy on unseen models by over 40% and 15% respectively.

II. RELATED WORK

A. Model Attribution

In essence, model attribution methods rely on some relationship between the internal states of generative models and the generated images. Depending on how such a relationship is created and identified, existing studies could be classified into three types: watermark-based methods, model-inversion-based methods, and fingerprint-based methods.

Watermarking has been widely used in copyright protection for digital contents [12], [13], database [14], [15], and recently, generative models [16]–[19]. Watermarking-based model attribution methods include those based on training data embedding [16], [17], weight modulation [18], [19], and latent vector watermarking [19]. Although watermarks facilitate model attribution, the injected watermark can hurt the quality of the generated images, besides, the attribution target is limited to models that have been watermarked, rather than any model, which limits its flexibility and application scenarios. Model-inversion-based methods [20]–[22] typically involves reversing the process to map an image back to its original latent space representation, followed by an attempt to regenerate the image. This technique is applicable only to white-box models, as it relies on accessing the model's parameters.

Fingerprint-based methods attribute models by identifying unique fingerprints on images of generative models, which are particularly evident in the spectrum. Compared to the two previously mentioned techniques, fingerprint-based model attribution approaches utilize the distinctive characteristics of generative models without requiring the injection of information into the model. They can be applied to both white-box and black-box models by relying solely on the output images. Marra et al. [5] used averaged noise residuals to represent model fingerprints and found that these fingerprints are periodic. Subsequent works [6], [8], [9] confirmed the existence of these fingerprints and achieved high accuracy with a fixed, finite set of models following a closed-set classification approach. Asnani et al. [23] extended this research to trace the

architectural components of models that generate images, which is beyond the scope of this paper. In open-world scenarios, with an unlimited number of unknown models, recent works [10], [11], [24] addressed model attribution using an open-set approach. However, the challenge of generalized model attribution remains unresolved. Current solutions are hampered by the seen/unseen imbalance issue in real-world scenarios, where only a limited number of seen models can be sampled while the number of unseen models continues to grow. Finding ways to improve the generalization performance of model attribution to new, emerging models remains a challenge.

B. Spectrum Discrepancies of Generative Models

Although fingerprints are visually imperceptible in the spatial domain, they are more noticeable in the frequency domain, often appearing as discrepancies in the spectrum. Existing studies [25]–[31] have sought to explain the spectrum discrepancies between generated and real images, particularly by studying the influence of upsampling and convolution layers.

Studies in [25]–[27] find that upsampling operations lead to high-frequency discrepancies between real and generated images. Zhang et al. [25] showed that the upsampling layer causes a periodic grid pattern on the spectrum. Durall et al. [26] identified a high-frequency discrepancy caused by the upsampling layer, which makes generative architectures struggle to fit the real image distribution. Schwarz et al. [27] discovered that different upsampling operations bias the generator toward distinct spectral properties. Other studies [28], [29] have analyzed the influence of convolution layers and attributed the frequency differences between real and generated images to the linear dependencies in the spectrum of convolutional filters, which hinder the learning of high frequencies.

The studies above primarily focused on differences between real and generated images, with fewer analyzing the frequency discrepancies between images generated by different models. In our study, we further investigate the influence of different types of activation and normalization layers and the effects of various convolution parameters. We have newly observed the influence of different generative blocks, providing additional insights into the formation of model fingerprints.

C. Pre-train on Synthetic Data

Our study is related to using the synthetic data for improving generalization performance. Baradad et al. [32] find that diverse noise data with capture certain structural properties of real data, despite far from realistic, could achieve good performance when used for self-supervised learning for a image classification task. Baek et al. [33] develop the data synthesis strategy by adopting the generic property of the natural images in power spectrum distribution, structure, and existence of saliency. The pretrained GANs using the synthetic dataset can effectively transfer in low-shot adaptation. Mishra et al. [34] propose a task-aware synthesis strategy to find the simulation parameters (lighting, pose, materials, etc.) that best fit the downstream task.

In contrast to these works, our research proposes synthesizing *models* rather than *images* to mimic the patterns of model fingerprints rather than natural images.

III. METHOD

In this work, our primary goal is to design a fingerprint extractor that could generalize to unseen models in the open world. To accomplish this goal, we propose a new approach by utilizing synthetic models, to mimic the fingerprint patterns of real-world generative models. By this approach, we significantly broaden the scope of the training data of fingerprint extractor, and consequently diminish the generalization gap. In the following, we begin with an analysis of the factors influencing the fingerprint patterns of generative models, detailed in Section III-A. Based the analysis, we then design our model synthesis strategy in Section III-B. Finally, in Section III-C, we use the synthetic models to train the fingerprint extractor to perform the model attribution task.

A. Preliminary Analysis of Model Fingerprint

Our study draws inspiration from recent research [5], [6], [31], which demonstrates that generative models, differing in architecture or parameters, leave unique patterns, termed *model fingerprints*, on their generated images. Despite these fingerprints are typically imperceptible in the spatial domain, they are more evident in the frequency domain. As shown in Figure 2, each generative model is characterized by a distinct pattern in the averaged Fourier spectrum. To gain insights for replicating these patterns, we first explore why generative models display unique spectrum patterns.

Our analysis mainly focuses on the generator (or decoder) part of CNN-based generative models. These generators produce images from either an encoded or a predefined latent vector. Typically, a generator comprises multiple generative blocks that transform the input latent vector into images. Common operations within the generative block involve components such as upsampling, convolution, normalization, and activation function. In the following, we aim to discuss the impact of these basic components and different generative blocks on the spectrum patterns of output images. Before the analysis, we first provide the background about analysis tools that will be employed in this section.

Background. Our analysis is based on the Discrete Fourier Transform (DFT). Specifically, for the input 2D image $I \in \mathbb{R}^{M \times N}$, the discrete Fourier transform for I is denoted by:

$$F(u, v) = \sum_{x=0}^{M-1} \sum_{y=0}^{N-1} I(x, y) \cdot e^{-i2\pi(ux/M+vy/N)},$$

for $u = 0, \dots, M-1, v = 0, \dots, N-1$

where $F(u, v)$ denotes the coefficient under the frequency component u and v , along the horizontal and vertical axis of the image. These coefficients consist of the so-called Fourier spectrum.

Sometimes, it is more convenient to consider the reduced 1D power spectrum [26], which is a simple yet characteristic 1D representation of the 2D Fourier spectrum. Technically, it is got by Azimuthal Integration (AI) over radial frequencies on the 2D Fourier spectrum:

$$AI(\omega) = \int_0^{2\pi} \|F(\omega \cdot \cos(\phi), \omega \cdot \sin(\phi))\|^2 d\phi, \quad (1)$$

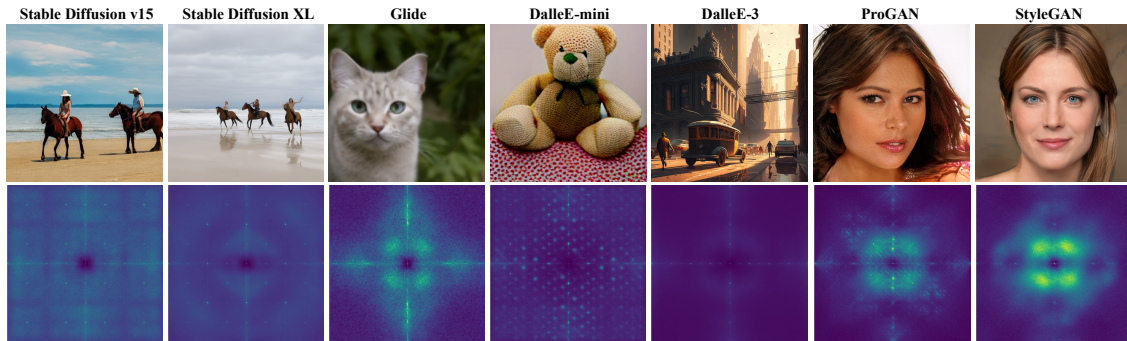


Fig. 2: Images (top) produced by generative models and the associated (averaged) Fourier spectrum (bottom). The unique characteristics of the Fourier spectrum can be regarded as the fingerprints of generative models and used for model attribution. The spectrum are obtained from high-pass filtered images processed through a denoiser.

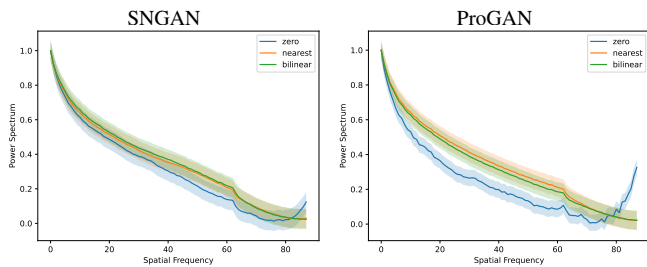


Fig. 3: Spectral effects of different types of upsampling layers.

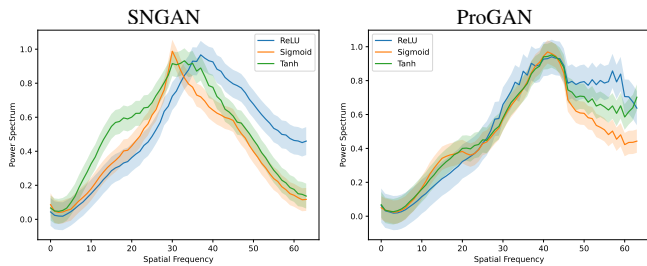


Fig. 4: Spectral effects of different types of activation functions.

where each value of $AI(\omega)$ represents the radial integral of the power over the 2D spectrum at a given radius ω . Consequently, the reduced 1D power spectrum effectively captures the distribution of different frequency components without regard to angular direction.

Network Components. We first study the *architecture* influences, including the types of three key architecture components: upsampling, activation function, and normalization. Subsequently, we discuss the *parameter* influences associated with convolution layers.

- **Upsampling Layers.** Upsampling layers serves to gradually increase the resolution of a generated image. Common types of upsampling layers are interpolation-based upsampler such as nearest and bilinear, and transposed convolution. Different types of upsampling are discussed in existing works to leave different spectral properties [25], [27]. To demonstrate this, we trained ProGAN [35] and SNGAN [36] models on the CelebA dataset, each with three types of upsampling layers. Figure 3 presents the

reduced 1D power spectrum of these models, where the x-axis indicates different frequencies from low to high, and the y-axis denotes the power of these frequency components. The figure illustrates that nearest and bilinear, which act as low-pass filters, significantly reduce high-frequency content, resulting in lower power at higher frequencies on the spectrum’s right side. In contrast, transposed convolution, which can be conceptualized as zero-interleaving followed by a convolution with a learnable kernel, tends to preserve more high-frequency components. This is because the learned convolution kernels in transposed convolution layers are not guaranteed to be low-pass, allowing more high-frequency artifacts to remain in the generated images [25].

- **Activation Function.** The choice of activation functions introduces non-linearities that shape the model’s frequency response. Different functions may enhance or suppress different aspects of the frequency spectrum. To verify this, we trained ProGAN and SNGAN models on the CelebA dataset, each with three different activation functions. As shown in Figure 4², generative models with ReLU activation generate images with more high-frequency components than Sigmoid and Tanh, as indicated by higher values on the right side of the reduced spectrum. The results may because that Tanh and Sigmoid compress the output into a bounded range, which has smooth properties and can damping high-frequency components. While ReLU is linear for all positive values, and zero otherwise, which allows high-frequency components to pass through unaffected in positive regions.
- **Normalization.** Normalization techniques adjust data within the network by normalizing based on calculated means and variances, which are computed differently depending on the method, such as across the entire batch for Batch Normalization [38] or for each individual sample in the case of Instance Normalization [39]. Despite employing similar mathematical formulations, these techniques could influence the network’s behavior

²To make the high-frequency discrepancy more evident, we first use a denoising filter by [37] with noise parameter $\sigma = 1$ to remove the low-frequency semantic contents.

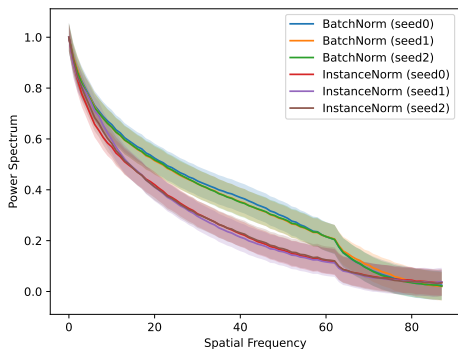


Fig. 5: Spectral effects of different types of normalization functions.

differently. Due to the variations in the optimization landscapes they create, different types of normalization may lead to distinctive distributions of parameters, and consequently different spectrum patterns. As demonstrated in Figure 5, we train six SNGAN models using two types of normalization, each type with three different initial seeds. As seen, models with the same normalization type often exhibit more consistent spectral patterns compared to those trained using different normalization methods. This underscores the impact of normalization choices on the diversity of spectrum patterns of generative models.

Convolution Parameters. Many factors, including optimization, initialization, and other configurations, can influence the parameters of a model. Our study primarily focuses on the parameters of convolution layers, which constitute a significant portion of a CNN-based model’s parameters. The shapes and sizes of convolution kernels critically determine how frequency components are handled. Different kernels can lead to different emphases on certain frequency bands, thus altering the model’s overall spectrum pattern. This phenomenon is illustrated in Figure 6, which shows the spectrum of two StyleGAN2 [40] models that have identical architecture but differ in their parameters, trained respectively on the FFHQ and FFHQu datasets. For this analysis, we extracted the parameters from a specific output channel in the last convolutional layer of each model’s final generative block. We then plot two figures for each model: the summed spectrum of the convolution kernels (left), and the spectrum of the output feature map for this channel (right). As demonstrated in the figure, for both models, the spectrum of the output feature map closely mirrors the spectrum of the convolution parameters. This alignment highlights how the convolutional layer’s kernel characteristics directly shape the spectrum pattern of the output.

Different Generative Blocks. The discussion above focuses on the influence of basic components. Moving forward, it is important to consider how different generative blocks throughout the entire generation process contribute to the final spectral pattern on the generate image. Generative models typically consist of multiple generative blocks, with upsampling layers playing a crucial role as connectors between these blocks, doubling the resolution of the input feature maps. As mentioned above, commonly used upsampling layers, such as bilinear and

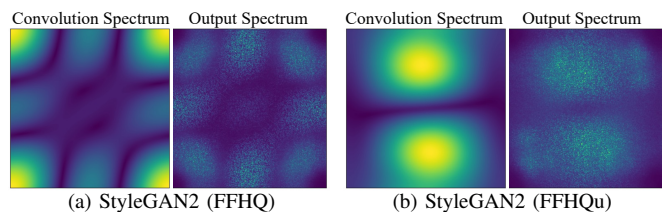


Fig. 6: Spectral effects of convolution parameters. This figure compares the summed spectrum of the convolution parameters with the spectrum of the output feature map.

nearest-neighbor interpolation, inherently possess a low-pass filtering effect. This property leads them to attenuate high-frequency components from prior layers. Given that existing research [6] suggesting that model fingerprints predominantly reside in the high-frequency components, it becomes apparent that the *later blocks in a model’s architecture could more significantly influence the model fingerprints on the output image as the high-frequency patterns from earlier layers could be filtered out*. To empirically test this hypothesis, we designed an experiment depicted in Figure 7, consisting of three key steps:

- **Training:** Train a classifier on the Fourier spectrum of images generated by two distinct generative models with the same architecture (Model 1 and Model 2).
- **Testing I:** Measure the classification results using a test set of images generated by Model 1 and Model 2.
- **Testing II:** Starting from the i -th block, sequentially exchange the succeeding blocks from Model 1 to Model 2 and vice versa. After each exchange, generate a new set of images with the composed models and assess the classifier’s classification results on this new dataset. Figure 7(c) visualize the operation by exchanging the last block.

Figure 7(d,e) shows the confusion matrices under Testing I and Testing II of two sets of experiments: one set on two ProGAN models utilizing nearest-neighbor upsampling (d), and the other set on two ProGAN models employing bilinear-upsampling (e). As shown in the Figure, under Testing I, the classifier achieves high accuracy, indicated by the high diagonal values in the confusion matrix. However, after swapping the last few blocks in Testing II, the confusion matrix reveals a notable reversal in model attribution results. The shifted results indicate that most distinguishable spectrum patterns used to differentiate the models are predominantly from the models’ last few blocks. And the patterns left by earlier blocks might be less pronounced as they progress through the generative process.

In summary, different generative models exhibit distinct spectral patterns due to both architectural and parameter-related factors, including the types of upsampling and activation functions employed, normalization techniques, and the parameters of convolution layers. Notably, our observations indicate that within the architecture of a large generative model, the final few blocks tend to have a more profound influence on the distinguishable spectral patterns of the output images.

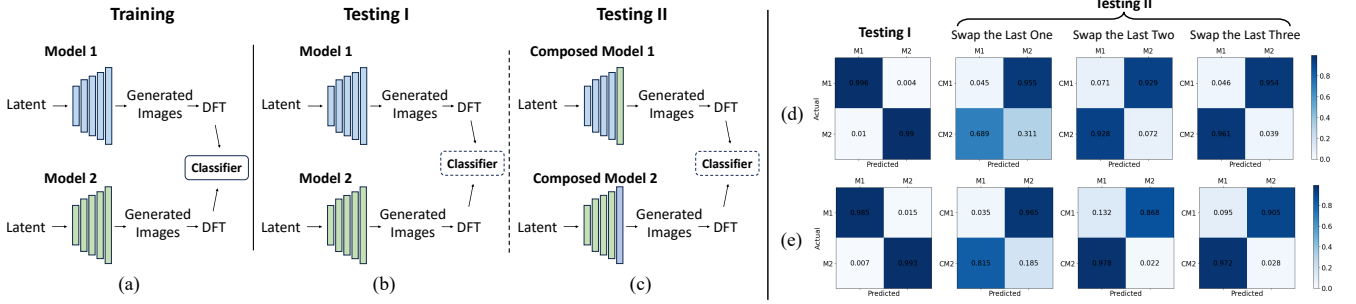


Fig. 7: (a-c) Verification of the importance of the last generative block in producing model fingerprints. In training (a), images generated by two models are used to train a 2-way classifier. In the first testing scenario (b), we test on non-overlap testing samples from the two models. In the second testing scenario (c), we test on samples from two composed models, which are constructed by switching the parameters of the last generative blocks of two models in training. (d-e) The confusion matrices in first and second testing scenarios. Model 1 and Model 2 are abbreviated as M1 and M2, respectively. Composed Model 1 and Composed Model 2 are abbreviated as CM1 and CM2.

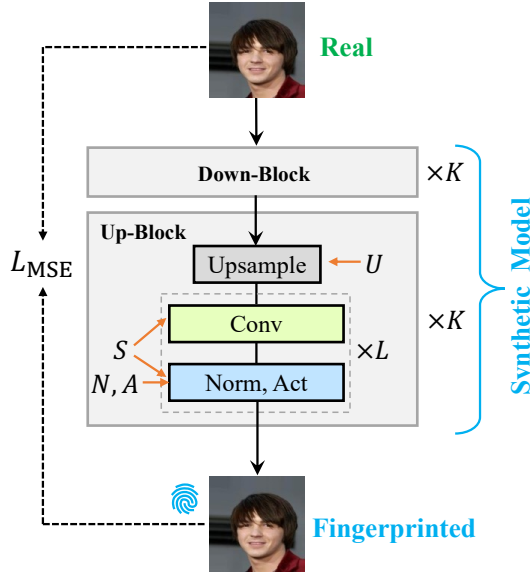


Fig. 8: Our proposed model synthesis strategy. The synthetic model receives a real image as input, producing a fingerprinted image that contains the distinct fingerprint characteristics associated with the synthetic model.

B. Model Synthesis Strategy

In this section, we introduce the model synthesis strategy that we use to create models for training the fingerprint feature extractor. Intuitively, a good synthesis strategy should generate models whose fingerprint patterns closely resemble those of real generative models, allowing these synthetic models to effectively simulate new models in an open environment. According to the discussion in Section III-A, there are important factors to consider. First, the last few blocks tend to have a more profound influence on the distinguishable spectrum patterns of the output images. Thus, employing a synthesis architecture with a small number of generative blocks could ensure fidelity in mimicking fingerprints. Second, it is crucial to increase diversity by varying the types of upsampling layers, activation

functions, normalization layers, and parameters. We explicitly incorporate these considerations into our method. Moreover, to further enhance diversity, we also consider variations in the number and sequence of layers.

Overall, our model synthesis strategy is illustrated in Figure 8, the structure of the synthetic model could be viewed as a shallow auto-encoder, composed of K downsampling blocks and K upsampling blocks. Based on the above discussion, K can be selected as a small value, such as one or two. Each downsampling block uses a fixed architecture, with a pooling layer to downscale the input resolution by half, and two convolutional layers to increase the feature dimension. The feature output from the downsampling blocks is then sent into the upsampling blocks, which share common components with the generative blocks in actual generative models and vary in many architecture options. The architecture of these blocks is defined by the options $\{U, A, N, L, S\}$.

- U is the upsampling operation that can be nearest neighbor upsampling, bilinear upsampling, or a stride 2 transposed convolution layer.
- A is the activation function that can be ReLU, Sigmoid, Tanh, or no activation.
- N is the normalization type that can be batch normalization, instance normalization, or no normalization.
- L represents the number of convolution layers in the block.
- S refers to the order of activation and normalization relative to the convolution layer.

By varying these configurations, we can get 288 different architectures within the construction space. For each architecture, we train M models with different training seeds, creating M distinct models with different parameters per architecture³.

We recognize that speed is a key factor in model synthesis. In our approach, we simplify the objective to focus on reconstruction, where the generative neural network is specifically tasked with minimizing the reconstruction loss of input images. This method is not only straightforward to implement but also allows for rapid training. We leave the exploration of other training approaches to future work. We set a constraint on the

³ M is set to 20 in our experiments.

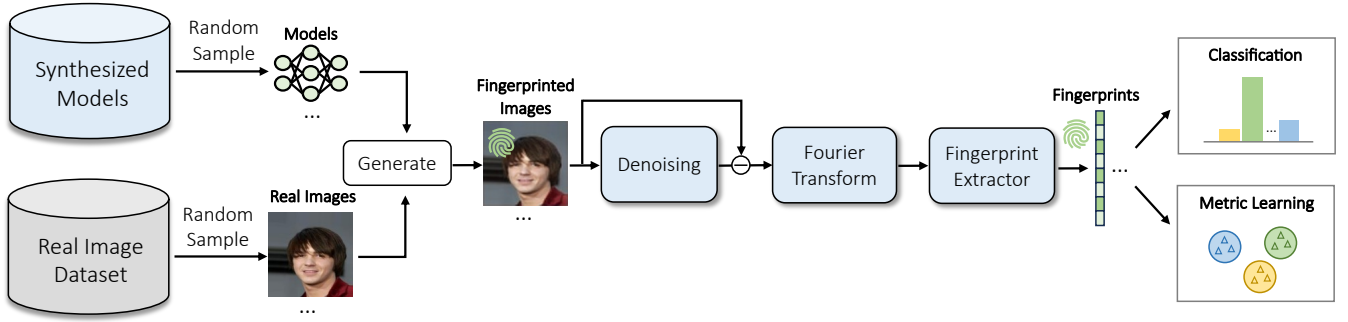


Fig. 9: Training the fingerprint extractor based-on synthetic models.

minimum reconstruction residual to $\eta = 0.005$ to limit the amount of artifacts in the output images. Ultimately, the total number of synthetic models generated is 5760, allowing for a wide simulation of a wide range of potential generative models with diverse architectures and parameters.

We measured the time required to train these models. For models with $K = 1$, the averaged required time per model is 53 seconds, while those with $K = 2$ required 113 seconds each. In total, training all the synthetic models takes 133 GPU hours on a single 3090 GPU. This is considerably more efficient than the time investment needed for training state-of-the-art generative models. For example, it takes 14 days 22 hours on single V100 GPUs to train a StyleGAN [41] model that generate with a 256×256 resolution⁴.

C. Training the Fingerprint Extractor

After obtaining the synthetic models, these models are utilized to train the fingerprint extractor. The goal of this extractor is to identify unique fingerprints embedded within images generated by different models, thereby enabling differentiation among them. As illustrated in Figure 9, the training procedure involves the synthetic model pool that we construct in the above section, and a real image dataset pool.

In the training phase, a batch of real images is randomly sampled from the real image dataset pool. Simultaneously, an equivalent number of synthetic models are selected from the synthetic model pool. Each real image I_{real} from the batch is processed through a synthetic model M_k , producing a generated image I_k that contains distinct fingerprints characteristic of the specific synthetic model used.

$$I_k = M_k(I_{\text{real}})$$

These generated images, now embedded with model-specific fingerprints, are subsequently processed by a denoiser by [37]. The primary function of this denoiser is to strip away low-frequency semantic content, thereby revealing the underlying high-frequency fingerprint patterns inherent in the images. The extracted noises are then transformed using a Discrete Fourier Transform to facilitate the extraction of their spectrum properties. The spectrum obtained from this transformation

are fed into the fingerprint extractor, which is built upon the ResNet50 architecture.

$$h_k = f_{\text{fp_extractor}}(\mathcal{F}(I'_k))$$

with $I'_k = I_k - f_{\text{denoise}}(I_k)$

where f_{denoise} and $f_{\text{fp_extractor}}$ denote the denoiser and fingerprint extractor, \mathcal{F} denotes the Discrete Fourier Transform, h_k is the extracted fingerprint embedding.

To enhance the model's performance, we combine classification and metric loss to enhance the discrimination of learned fingerprint embedding. The classification head employs a multi-class cross-entropy (CE) loss function, which enable the fingerprint extractor to accurately classify the originating synthetic model of each input image. The projection head is followed by a triplet loss, which encourages generated images from the same generator to be as similar as possible in the feature space while promoting a larger dissimilarity between images from different generators.

$$\mathcal{L} = \mathcal{L}_{\text{CE}}(h_k, y_k) + \mathcal{L}_{\text{Triplet}}(h_a, h_p, h_n)$$

where y_k is the true label for k -th synthetic model. h_a , h_p , and h_n are the anchor, positive, and negative fingerprint embedding from a triplet set.

IV. EXPERIMENTS

In the experimental section, we aim to answer the following evaluation questions:

- EQ1** How is the fidelity and diversity of synthetic models?
- EQ2** How do the synthesis, training, and inference options affect the generalization ability of the fingerprint extractor?
- EQ3** How does our method perform compared with existing methods in model identification and verification scenarios?
- EQ4** Can we apply the trained fingerprint extractor in more complex attribution tasks, such as model lineage analysis?

A. Experimental Details

Testing Models. Although our analysis and synthesis strategy primarily focuses on CNN-based generative models, our evaluation includes a broader scope of models as shown in Table I. In addition to CNN-based models, we also assess the generalization performance on Transformer-based models,

⁴<https://github.com/NVlabs/stylegan>

TABLE I: Models highlighted in gray are considered classical models and are used to train the existing methods being compared. The remaining models are categorized as emerging models and have not been seen by the existing methods.

Category	Type	Image Source	Res.	Models
CNN-based	GAN	CelebA	128	ProGAN [35], MMDGAN [42], SNGAN [43], StarGAN [44], AtGAN [45]
		CelebAHQ/FFHQ	1024	ProGAN, StyleGAN [41], StyleGAN2 [40], StyleGAN3-i [46], StyleGAN3-r [46]
	VAE	CelebA	64	VanillaVAE [47], BetaVAE [48], DisentangledBetaVAE [49], InfoVAE [50]
	Flow	CelebA	128	ResFlow [51], Glow [52]
	Diffusion	Lsun-Bedroom	256	ADM [53], DDPM [54], LDM [3], PDNM [55]
Transformer-based	GAN	FFHQ	256	GANsformer [56], StyleSwin [57]
		CelebA	64	TransGAN [58], Styleformer [59]
Text2Image Models	-	-	-	SD1.5 [3], SD2.1, SDXL, MJ [4], Glide [1], DalleE-mini [60], DalleE-2 [2], DalleE-3 [61]

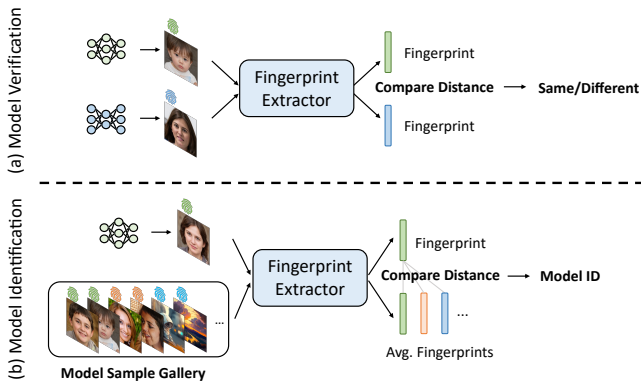


Fig. 10: Illustration of the model verification (above) and identification (below) problem.

which share many common components with CNN-based models. And for CNN-based category, we include a variety of models such as CNN, VAE, Flow, and Diffusion models. All models in the CNN-based and Transformer-based category are unconditional models, which are trained on the dataset in the “Image Source” column with different resolutions. Furthermore, the last row of the table encompasses state-of-the-art Text2Image models such as Stable Diffusion v1.5, Stable Diffusion v2.1, Stable Diffusion XL, Glide, DalleE-mini, DalleE-2, and DalleE-3. These models are not restricted to specific domains, and diverse in architecture type, training dataset, and resolution.

For the ablation study in Section IV-C, our fingerprint extractor is purely trained on synthetic models, all models in the table are unseen. For the comparisons with existing methods in Section IV-D, certain models highlighted in gray are used for training existing methods, and a fine-tuned version of our method pre-trained on synthetic models.

Experimental Setup. Similar to the face identification and verification problems encountered in the field of face recognition, we consider two model attribution problems, the 1:1 model verification and 1:N model identification problem, as shown in Figure 10. Settings and experimental setups for the two problems are illustrated below:

- **Model Verification:** the 1:1 model verification problem aims to verify whether two generated images are from the

same model or not. Model verification is performed by comparing the similarity of the extracted fingerprint. To assess the performance, we generate 1,000 images for each model under test. Then we randomly selected 10,000 pairs out of these images, which consist of 5,000 negative pairs (images from different models) and 5,000 positive pairs (images from the same model). The evaluation employs metrics commonly used in face verification tasks: accuracy and the Area Under the Receiver Operating Characteristic Curve (AUC). Accuracy measures the correct verification of pairs as originating from the same or different models. We report the best accuracy across all similarity thresholds to assess the overall effectiveness of the verification system. The AUC provides a comprehensive measure of performance across all possible threshold levels, reflecting the trade-off between the true positive rate and the false positive rate.

- **Model Identification:** the 1:N model identification problem aims to identify the specific generative model used to create a given image among N models. To assess the performance of model identification, we generate 1,000 images for each model under test. Out of these, 10 images are sampled to create the fingerprint for each model, while the rest serve as test samples. Each model’s fingerprint is collected to form the model gallery. We compare the test sample with each fingerprint in the gallery and classify it to the class with the closest fingerprint distance. Performance is evaluated using classification accuracy and the F1 score.

Compared methods. To compare with existing methods, we derive two variants of our method: 1) *Ours (Only-Syn)*, which is only trained on synthetic models without having seen any real models in Table I. 2) *Ours (Fine-tune)*, which fine-tune the fingerprint extractor trained on synthetic models for one epoch using samples of models highlighted in gray in the table.

We compare against five existing model attribution methods. They are Marra et al. [5], Yu et al. [6], DNA-Det [8], RepMIX [9], and POSE [10]. For the training-based methods among these, we train them on models in gray in Table I. Then we extract the layers before the classification head as the fingerprint extractor. This adaptation is implemented to evaluate the model identification and verification problems.

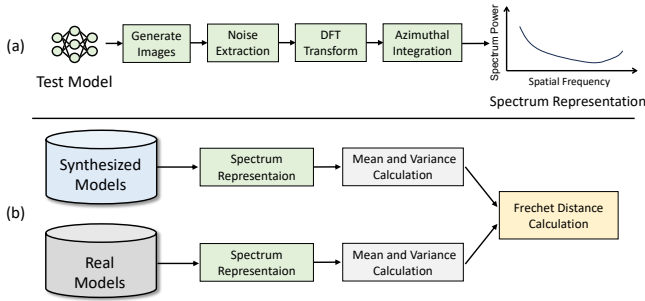


Fig. 11: (a) Spectrum pattern representation on a single model. (b) The calculation process of Fréchet Frequency Distance.

TABLE II: Compare the synthesis fidelity when using all synthesis models and reducing each synthesis option.

Models	All	w/o K	w/o L	w/o S
FFD	3.30	3.57	3.41	3.51
Models	w/o U	w/o A	w/o N	w/o seed
FFD	9.81	4.46	3.02	3.39

B. Effectiveness of Model Synthesis (EQ1)

The generalization capability of our trained fingerprint extractor is built upon synthetic models. Before evaluating the fingerprint extractor, we first conduct evaluations on the synthetic models in two crucial dimensions: 1) *Fidelity*, which assesses the extent how well the synthetic models replicate the spectrum/fingerprint patterns of real models. 2) *Diversity*, which examine whether the synthetic models exhibit a wide range of spectrum patterns, rather than merely replicating a limited set.

Fidelity. Currently, there is no off-the-shelf tool to quantitatively measure the gap between synthetic and real models in fingerprint distributions. To address this gap, we introduce a new metric called Fréchet Frequency Distance (FFD), inspired by the Fréchet Inception Distance (FID) [62] commonly used to assess the quality of images from generative models. The FFD is calculated through two primary steps:

- **(Step I) Spectrum Pattern Representation:** We extract the spectrum pattern of generated images to represent the fingerprint pattern of each synthesized and real models. As depicted in Figure 11(a), for each model, we initially generate N (e.g., 100) images, and then, following [31], we enhance the spectrum patterns by applying a noise extractor [37] to remove semantic contents from these images. The resultant noise images are then used to compute a reduced 1D power spectrum, as specified in Equation (1). We calculate the averaged spectrum from these N images to serve as the spectrum pattern representation for each model.
- **(Step II) Fréchet Distance Calculation:** As illustrated in Figure 11(b), we first compute the mean and covariance of the spectrum representations for real models in Table I, and synthetic models in Section III-B. The Fréchet distance is then calculated between these distributions. Specifically, for the mean μ_r and covariance Σ_r of real distribution, and

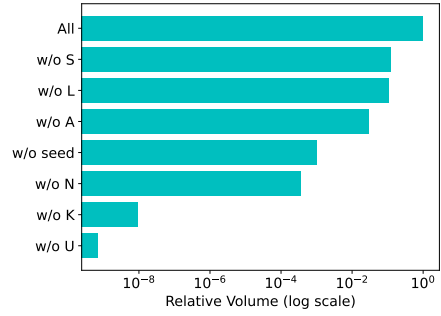


Fig. 12: Compare the relative proportions of volume against the total volume of all synthesized models when reducing each synthesis option.

TABLE III: Ablation study on the architecture of synthetic models.

Syn Models	Verification		Identification	
	Acc	AUC	Acc	F1
w/o K (K=1)	87.04	94.57	92.69	92.51
w/o L (L=1)	87.54	95.08	90.04	89.86
w/o S (conv-norm-act)	89.29	95.56	93.91	93.75
w/o U (bilinear)	87.68	94.18	88.96	88.64
w/o A (no act)	84.75	92.19	87.03	86.80
w/o N (no norm)	87.63	94.80	93.47	93.40
All	89.73	95.69	94.03	93.84

the mean μ_s and covariance Σ_s of synthetic distribution, their distance is given by:

$$\text{FFD} = \|\mu_r - \mu_s\|^2 + \text{Tr} \left(\Sigma_r + \Sigma_s - 2(\Sigma_r \Sigma_s)^{1/2} \right),$$

where Tr represents the trace of a matrix. A low FFD score indicates that the synthetic models closely mimic the real models in terms of spectrum patterns.

In Table II, we evaluate the Fréchet Frequency Distance of synthetic models against real models, varying synthesis choices. The variations in the architecture include: “w/o K” and “w/o L,” indicating the construction with a single down/up block and a single layer, respectively; “w/o S,” using only one type of sequence — normalization and activation after convolution; “w/o U,” utilizing only bilinear interpolation for upsampling; and “w/o A” and “w/o N,” which denote the absence of activation and normalization layers, respectively. We also consider not using diverse seeds for each architecture, denoted as “w/o seed”. The results displayed in the table indicate that reducing most synthesis options tends to increase the Fréchet Frequency Distance (FFD), pointing to a poorer alignment between the distributions. Notably, eliminating the diversity in activation functions and upsampling methods results in the most significant increases in FFD. This may be because these factors, when varied, typically enhance the spectrum resemblance to real distributions.

Diversity. Although the FFD score effectively compares the fingerprint resemblance to the real models in Table I, the limited size of the real model dataset might prevent it from fully capturing the diversity of the synthetic data, potentially resulting in a bias toward the limited variety seen in the real

TABLE IV: Ablation study on the number of seeds to train models based on each synthetic architecture.

Seed Num	Verification		Identification	
	Acc	AUC	Acc	F1
1	89.87	96.11	91.04	90.89
10	88.00	94.70	93.03	92.87
15	88.87	95.37	93.96	93.78
20	89.73	95.69	94.03	93.84

TABLE V: Ablation study on the real dataset for fingerprinted image generation based-on synthetic models.

Real Dataset	Verification		Identification	
	Acc	AUC	Acc	F1
CelebA	87.50	94.60	93.90	93.78
LSUN	89.72	95.53	93.62	93.48
CelebA + LSUN	89.73	95.69	94.03	93.84

dataset. Therefore, we propose using an additional metric, the Volume of Confidence Ellipsoid [63], to better assess the extent to which the synthetic models occupy the spectrum representation space. The volume is calculated as follows:

$$\text{Volume} = \frac{(2\pi)^{n/2}}{\Gamma\left(\frac{n}{2} + 1\right)} \times \sqrt{\prod_{i=1}^n \lambda_i},$$

where λ_i are the eigenvalues of the covariance matrix of spectrum representations of all synthetic models, n is the number of dimensions, and Γ denotes the gamma function. This formula determines the volume of an ellipsoid in n -dimensional Euclidean space.

Figure 12 displays the relative volume proportions obtained by removing each synthesis option compared to the total volume of all synthesized models. As seen in the table, removing any synthesis option reduces the volume of the spectrum representation, with proportions smaller than 1. This suggests that incorporating all variations enhances the diversity of synthesized models.

C. Ablation Study (EQ2)

In the ablation study section, we examine several key factors affecting the generalization performance of the fingerprint extractor. These factors include: the types of synthetic models and real images used for creating fingerprinted images, the selection of input signals extracted from these fingerprinted images for training the fingerprint extractor, and the implementation of a sliding window strategy during the inference phase. This comprehensive evaluation helps in understanding how each component contributes to the effectiveness of the fingerprint extraction. Note that in this section, the fingerprint extractor is trained only on synthetic models and evaluated on all the models in Table I, without including any real generative models in training. Our default configurations within the tables are highlighted in gray.

Synthetic Models. To evaluate the impact of individual synthesis options of synthetic models on the generalization

TABLE VI: Ablation study on the input image for fingerprint extraction.

Input Image	Verification		Identification	
	Acc	AUC	Acc	F1
RGB	79.22	87.42	60.33	59.71
Spectrum	83.09	90.76	73.94	74.44
Noise Spectrum	89.73	95.69	94.03	93.84

TABLE VII: Ablation study on the sliding window.

Slide Strategy	Verification		Identification	
	Acc	AUC	Acc	F1
w/o slide window	88.42	94.63	87.92	87.68
2×2 slide window	89.88	95.38	91.84	91.79
3×3 slide window	89.73	95.69	94.03	93.84
4×4 slide window	89.68	95.60	94.03	93.81

of the trained fingerprint extractor in model verification and identification tasks, we conducted an ablation study. The results, presented in Table III, demonstrate that omitting any synthesis option reduces the generalization capabilities in model identification and verification tasks. Notably, the removal of the upsampling and activation layers significantly affects generalization performance. This observation aligns with the Fréchet Frequency Distance scores listed in Table II, where the absence of activation and upsampling variation results in the highest scores, indicating the lowest fidelity of synthetic models.

Real Dataset. In Table V, we evaluate how the choice of real datasets used to generate fingerprinted images with synthetic models affects the generalization performance of the trained fingerprint extractor. We consider three options for constructing the real image pool: the CelebA dataset, which exclusively contains face images; the LSUN dataset, featuring 20 different types of semantic images; and a composite of both datasets. The results indicate that the combination of the CelebA and LSUN datasets, which offers the richest semantic diversity, yields the best generalization performance. This phenomenon may be because the increasing the semantic diversity of fingerprinted images helps the fingerprint extractor focus on semantic-agnostic fingerprint features.

Input Signal. In Table VI, we assess the impact of different input signals extracted from fingerprinted images on the training of the fingerprint extractor. We consider three types of inputs: the RGB image directly, the DFT spectrum of the RGB image (Spectrum), and the DFT spectrum of the noise extracted from the RGB image (Noise Spectrum). The noise is extracted using a denoising process that primarily removes high-level semantic details from the image. As demonstrated in the table, the choice of input signal significantly affects the generalization ability of the fingerprint extractor. The "Noise Spectrum" input yields the best performance, followed by "Spectrum," with the direct RGB image showing the least effectiveness. This outcome suggests that the Noise Spectrum most effectively enhances the high-frequency fingerprint information within the image, making the fingerprint features more extractable and distinct.

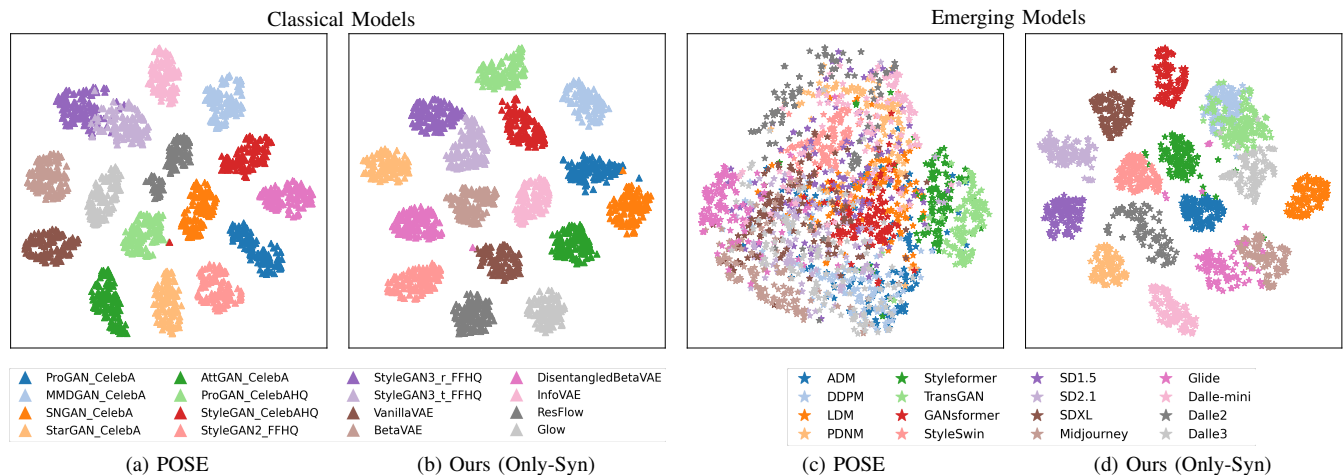


Fig. 13: Compare existing method POSE [10] and our method in attributing classical and emerging models. POSE is trained on samples from classical models. As depicted in the figure, it effectively extracts distinct fingerprint patterns from these seen models (a), while struggles to generalize this capability to unseen, emerging models (c). In contrast, our method, despite not being trained on any of these testing models, demonstrates robust generalization abilities on the two groups of models (b,d).

TABLE VIII: Performance comparison of model identification.

Method	Classical Models		Emerging Models	
	Acc	F1	Acc	F1
Marra et al. [5]	61.00	55.01	26.72	22.33
Yu et al. [6]	96.28	96.27	31.93	30.67
DNA-Det [8]	98.55	98.55	47.41	46.60
RepMix [9]	94.34	94.29	26.63	25.35
POSE [10]	<u>98.93</u>	<u>98.93</u>	49.80	48.87
Ours (Only-Syn)	96.71	96.70	<u>93.20</u>	<u>93.11</u>
Ours (Fine-tune)	99.88	99.89	94.02	93.97

TABLE IX: Performance comparison of model verification.

Method	Classical Models		Emerging Models	
	Acc	AUC	Acc	AUC
Marra et al. [5]	66.10	68.99	59.37	59.46
Yu et al. [6]	96.80	99.27	63.84	68.97
DNA-Det [8]	99.31	99.94	69.64	77.54
RepMix [9]	99.15	97.44	61.09	57.92
POSE [10]	98.76	99.91	66.94	72.85
Ours (Only-Syn)	92.01	96.90	85.88	92.66
Ours (Fine-tune)	<u>99.21</u>	<u>99.93</u>	<u>85.62</u>	<u>92.55</u>

Sliding Window. During the inference phase for extracting fingerprints from test images of varying resolutions, we implement a sliding window strategy to accommodate different input sizes. The training resolution for the fingerprint extractor is set at 128×128 pixels. For testing images that exceed this resolution, we employ an equally spaced sliding window technique to divide the image into $N \times N$ patches, each with 128×128 pixels. These patches are then individually processed to extract fingerprints. The final fingerprint for the entire input image is obtained by averaging the fingerprints from all these patches, ensuring comprehensive coverage and utilization of the image’s information for accurate fingerprint extraction. For images with resolutions smaller than 128×128 , we resize them to the required 128×128 resolution. As indicated in Table VII, the sliding window strategy significantly enhances model identification performance. This improvement is attributed to the strategy’s ability to capture a richer set of fingerprint information within the test image. Given that the performance of 3×3 and 4×4 sliding configurations shows similar results, we use the 3×3 configuration for inference efficiency.

D. Comparison with Existing Methods (EQ3)

Model Identification In Table VIII, we evaluate and compare our methods—Ours (Only-Syn) and Ours (Fine-tune)—against

existing methods in the 1:N model identification scenario. The results show that most existing methods achieve high identification accuracy on classical models, which are seen in their training. However, their performance significantly declines when tested on unseen emerging models, dropping below 50%. In contrast, our method “Ours (Only-Syn)” demonstrates strong generalization capabilities. Despite being trained only on synthesized models and not having exposure to real generative models, it achieves over 90% identification accuracy on the two sets of models. To align more closely with existing methods, we introduce “Ours (Fine-tune),” which is further fine-tuned using classical model images. This adjustment improves the identification accuracy to 99% on classical models, with a modest enhancement on emerging models. These results underscore that our fingerprint extractor, by leveraging synthetic models, exhibits superior generalization ability across real-world generative models due to its exposure to a broader model fingerprint variations. Figure 13 visualizing the extracted fingerprint embeddings also indicates this.

Model Verification. In Table IX, we compare our methods against existing methods in the 1:1 model verification scenario, which involves determining whether two input images are generated by the same model. Similar to the findings in the 1:N model identification scenario, existing methods exhibit

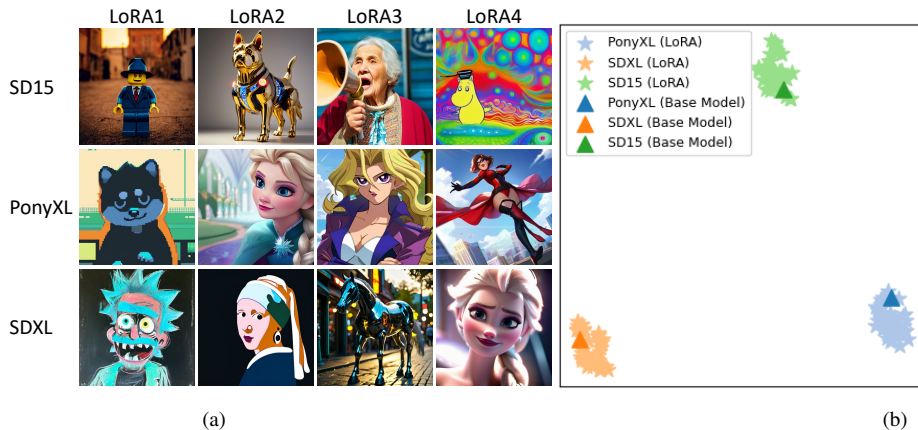


Fig. 14: (a) Images Generated by Different LoRA-Equipped Models: We collect four distinct LoRA weights for each of the three Base Models: SD15, PonyXL, and SDXL. (b) t-SNE visualization of the fingerprint embeddings of the three Base Models, alongside generated images by their corresponding LoRA-equipped variants.

high verification accuracy for seen models but show significant performance degradation when applied to unseen models. Our method, Ours (Only-Syn), trained solely on synthetic models, demonstrates balanced performance across the two groups of model. This indicates a robust ability to generalize from synthetic model to real-world generative models. When we fine-tune the fingerprint extractor with images from classical models, as in Ours (Fine-tune), the performance on classical models is up to par with existing methods while maintaining superior performance on unseen emerging models.

E. Model Lineage Analysis (EQ4)

At times, models may be stolen and utilized as the base model for training variants by other entities. Our model fingerprint extractor (Only-Syn) demonstrates the potential to trace back to the base model of such variants. To illustrate this capability, we gathered models from Civitai⁵, a community renowned for its vast repository of high-quality Stable Diffusion models. The majority of these models are LoRA-variant models, fine-tuned from a base model using LoRA (Low-Rank Adaption) [64]. We collected four distinct LoRA weights for each of the three most commonly used base models: SD15, PonyXL v6, and SDXL 1.0. Subsequently, we generated 10 images for each LoRA-equipped model and base model. Figure 14(a) show the generated images by these LoRA variants, which exhibit discernible differences in styles and semantics. We employing the averaged fingerprint of generated images as the fingerprint for the base model. As shown in Figure 14(b), the LoRA-equipped variants exhibit similar fingerprint embeddings with their respective base models. This result shows that we could easily attribute the LoRA variant to its base model comparing the extracting fingerprints from their generated images.

V. CONCLUSIONS AND FUTURE WORK

In this paper, we propose to tackle the model attribution problem in a more generalized scenario, to expand the attribu-

tion target to unseen models that are not included in training. To solve the problem, we propose a novel method by training on a large and diverse set of synthetic models, which mimic the fingerprint patterns of real generative models. The synthesis strategy is based a detailed analysis of how different model architectures and parameters influence fingerprint patterns, and is validated using two designed metrics to assess their fidelity and diversity. Experimental results demonstrate that our fingerprint extractor, trained on synthetic models, exhibits superior generalization capabilities in identifying and verifying unseen real generative models across various scenarios.

Beyond the scope of this paper, there are several promising directions worth further explorations. Firstly, the generated images may undergo subsequent processing in practical scenarios, which can diminish their intrinsic spectrum patterns. It is important to develop methods for extracting robust patterns to prepare the fingerprint extractor for more practical applications. Secondly, aside from LoRA, there are many other types of model variants derived from a base model. Exploring more relationships between models through fingerprint extraction holds potential for researchers. Finally, while our method has shown effective generalization ability of training solely on synthetic models and tested on real models without fine-tuning, it does not outperform the performance of directly training on real models and test on these models. This indicates that the potential of model synthesizing has not been fully exploited. How to further increase the fidelity and diversity of model synthesis is also an important research direction in the future.

REFERENCES

- [1] A. Nichol, P. Dhariwal, A. Ramesh, P. Shyam, P. Mishkin, B. McGrew, I. Sutskever, and M. Chen, “Glide: Towards photorealistic image generation and editing with text-guided diffusion models,” in *ICML*, 2021.
- [2] A. Ramesh, P. Dhariwal, A. Nichol, C. Chu, and M. Chen, “Hierarchical text-conditional image generation with clip latents,” *arXiv preprint arXiv:2204.06125*, 2022.
- [3] R. Rombach, A. Blattmann, D. Lorenz, P. Esser, and B. Ommer, “High-resolution image synthesis with latent diffusion models,” in *CVPR*, 2022.
- [4] “Midjourney,” <https://www.midjourney.com>.

⁵<https://civitai.com/>

- [5] F. Marra, D. Gragnaniello, L. Verdoliva, and G. Poggi, "Do gans leave artificial fingerprints?" in *MIPR*, 2019.
- [6] N. Yu, L. S. Davis, and M. Fritz, "Attributing fake images to gans: Learning and analyzing gan fingerprints," in *ICCV*, 2019.
- [7] X. Xuan, B. Peng, W. Wang, and J. Dong, "Scalable fine-grained generated image classification based on deep metric learning," *arXiv preprint arXiv:1912.11082*, 2019.
- [8] T. Yang, Z. Huang, J. Cao, L. Li, and X. Li, "Deepfake network architecture attribution," in *AAAI*, 2022.
- [9] T. Bui, N. Yu, and J. Collomosse, "Repmix: Representation mixing for robust attribution of synthesized images," in *ECCV*, 2022.
- [10] T. Yang, D. Wang, F. Tang, X. Zhao, J. Cao, and S. Tang, "Progressive open space expansion for open-set model attribution," in *CVPR*, 2023.
- [11] L. Abady, J. Wang, B. Tondi, and M. Barni, "A siamese-based verification system for open-set architecture attribution of synthetic images," *Pattern Recognition Letters*, 2024.
- [12] I. Cox, M. Miller, J. Bloom, and C. Honsinger, "Digital watermarking," *Journal of Electronic Imaging*, vol. 11, no. 3, pp. 414–414, 2002.
- [13] F. Hartung and M. Kutter, "Multimedia watermarking techniques," *Proceedings of the IEEE*, vol. 87, no. 7, pp. 1079–1107, 1999.
- [14] D. Hu, D. Zhao, and S. Zheng, "A new robust approach for reversible database watermarking with distortion control," *IEEE Transactions on Knowledge and Data Engineering*, vol. 31, no. 6, pp. 1024–1037, 2018.
- [15] Z. Ren, H. Fang, J. Zhang, Z. Ma, R. Lin, W. Zhang, and N. Yu, "A robust database watermarking scheme that preserves statistical characteristics," *IEEE Transactions on Knowledge and Data Engineering*, 2023.
- [16] N. Yu, V. Skripniuk, S. Abdelnabi, and M. Fritz, "Artificial gan fingerprints: Rooting deepfake attribution in training data," in *ICCV*, 2021.
- [17] Y. Zhao, T. Pang, C. Du, X. Yang, N.-M. Cheung, and M. Lin, "A recipe for watermarking diffusion models," *arXiv preprint arXiv:2303.10137*, 2023.
- [18] N. Yu, V. Skripniuk, D. Chen, L. Davis, and M. Fritz, "Responsible disclosure of generative models using scalable fingerprinting," in *ICLR*, 2022.
- [19] G. Nie, C. Kim, Y. Yang, and Y. Ren, "Attributing image generative models using latent fingerprints," 2023.
- [20] M. Albright and S. McCloskey, "Source generator attribution via inversion," in *CVPR Workshops*, vol. 8, 2019, p. 3.
- [21] B. Zhang, J. P. Zhou, I. Shumailov, and N. Papernot, "On attribution of deepfakes," *arXiv preprint arXiv:2008.09194*, 2020.
- [22] M. Laszkiewicz, J. Ricker, J. Lederer, and A. Fischer, "Single-model attribution via final-layer inversion," *arXiv preprint arXiv:2306.06210*, 2023.
- [23] V. Asnani, X. Yin, T. Hassner, and X. Liu, "Reverse engineering of generative models: Inferring model hyperparameters from generated images," 2023.
- [24] S. Girish, S. Suri, S. S. Rambhatla, and A. Shrivastava, "Towards discovery and attribution of open-world gan generated images," in *ICCV*, 2021.
- [25] X. Zhang, S. Karaman, and S.-F. Chang, "Detecting and simulating artifacts in gan fake images," in *WIFS*. IEEE, 2019.
- [26] R. Durall, M. Keuper, and J. Keuper, "Watch your up-convolution: Cnn based generative deep neural networks are failing to reproduce spectral distributions," in *CVPR*, 2020.
- [27] K. Schwarz, Y. Liao, and A. Geiger, "On the frequency bias of generative models," in *NeurIPS*, 2021.
- [28] T. Dzanic, K. Shah, and F. Witherden, "Fourier spectrum discrepancies in deep network generated images," in *NeurIPS*, 2020.
- [29] M. Khayatkhoie and A. Elgammal, "Spatial frequency bias in convolutional generative adversarial networks," in *AAAI*, 2022.
- [30] K. Chandrasegaran, N.-T. Tran, and N.-M. Cheung, "A closer look at fourier spectrum discrepancies for cnn-generated images detection," in *CVPR*, 2021.
- [31] R. Corvi, D. Cozzolino, G. Poggi, K. Nagano, and L. Verdoliva, "Intriguing properties of synthetic images: from generative adversarial networks to diffusion models," in *Proceedings of the IEEE/CVF Conference on Computer Vision and Pattern Recognition*, 2023, pp. 973–982.
- [32] M. Baradad Jurjo, J. Wulff, T. Wang, P. Isola, and A. Torralba, "Learning to see by looking at noise," in *NeurIPS*, 2021.
- [33] K. Baek and H. Shim, "Commonality in natural images rescues gans: Pretraining gans with generic and privacy-free synthetic data," in *Proceedings of the IEEE/CVF Conference on Computer Vision and Pattern Recognition*, 2022, pp. 7854–7864.
- [34] S. Mishra, R. Panda, C. P. Phoo, C.-F. R. Chen, L. Karlinsky, K. Saenko, V. Saligrama, and R. S. Feris, "Task2sim: Towards effective pre-training and transfer from synthetic data," in *Proceedings of the IEEE/CVF conference on computer vision and pattern recognition*, 2022, pp. 9194–9204.
- [35] T. Karras, T. Aila, S. Laine, and J. Lehtinen, "Progressive growing of gans for improved quality, stability, and variation," in *ICLR*, 2018.
- [36] T. Miyato, T. Kataoka, M. Koyama, and Y. Yoshida, "Spectral normalization for generative adversarial networks," in *ICLR*, 2018.
- [37] K. Zhang, W. Zuo, Y. Chen, D. Meng, and L. Zhang, "Beyond a gaussian denoiser: Residual learning of deep cnn for image denoising," *IEEE transactions on image processing*, vol. 26, no. 7, pp. 3142–3155, 2017.
- [38] S. Ioffe and C. Szegedy, "Batch normalization: Accelerating deep network training by reducing internal covariate shift," in *International conference on machine learning*. pmlr, 2015, pp. 448–456.
- [39] D. Ulyanov, A. Vedaldi, and V. Lempitsky, "Instance normalization: The missing ingredient for fast stylization," *arXiv preprint arXiv:1607.08022*, 2016.
- [40] T. Karras, S. Laine, M. Aittala, J. Hellsten, J. Lehtinen, and T. Aila, "Analyzing and improving the image quality of stylegan," in *CVPR*, 2020.
- [41] T. Karras, S. Laine, and T. Aila, "A style-based generator architecture for generative adversarial networks," in *CVPR*, 2019.
- [42] M. Bińkowski, D. J. Sutherland, M. Arbel, and A. Gretton, "Demystifying MMD GANs," in *ICLR*, 2018.
- [43] H. Zhang, I. Goodfellow, D. Metaxas, and A. Odena, "Self-attention generative adversarial networks," in *ICML*, 2019.
- [44] Y. Choi, M. Choi, M. Kim, J.-W. Ha, S. Kim, and J. Choo, "Stargan: Unified generative adversarial networks for multi-domain image-to-image translation," in *CVPR*, 2018.
- [45] Z. He, W. Zuo, M. Kan, S. Shan, and X. Chen, "Attgan: Facial attribute editing by only changing what you want," *TIP*, vol. 28, no. 11, pp. 5464–5478, 2019.
- [46] T. Karras, M. Aittala, S. Laine, E. Härkönen, J. Hellsten, J. Lehtinen, and T. Aila, "Alias-free generative adversarial networks," in *NeurIPS*, 2021.
- [47] D. P. Kingma and M. Welling, "Auto-encoding variational bayes," in *ICLR*, 2014.
- [48] I. Higgins, L. Matthey, A. Pal, C. Burgess, X. Glorot, M. Botvinick, S. Mohamed, and A. Lerchner, "beta-vae: Learning basic visual concepts with a constrained variational framework," in *ICLR*, 2017.
- [49] C. P. Burgess, I. Higgins, A. Pal, L. Matthey, N. Watters, G. Desjardins, and A. Lerchner, "Understanding disentangling in beta-vae," in *NIPS workshop*, 2017.
- [50] S. Zhao, J. Song, and S. Ermon, "Infovae: Information maximizing variational autoencoders," *arXiv preprint arXiv:1706.02262*, 2017.
- [51] R. T. Chen, J. Behrmann, D. K. Duvenaud, and J.-H. Jacobsen, "Residual flows for invertible generative modeling," in *NeurIPS*, 2019.
- [52] D. P. Kingma and P. Dhariwal, "Glow: Generative flow with invertible 1x1 convolutions," in *NeurIPS*, 2018.
- [53] P. Dhariwal and A. Nichol, "Diffusion models beat gans on image synthesis," in *NeurIPS*, 2021.
- [54] J. Ho, A. Jain, and P. Abbeel, "Denoising diffusion probabilistic models," in *NeurIPS*, 2020.
- [55] L. Liu, Y. Ren, Z. Lin, and Z. Zhao, "Pseudo numerical methods for diffusion models on manifolds," in *ICLR*, 2022.
- [56] D. A. Hudson and L. Zitnick, "Generative adversarial transformers," in *ICML*, 2021.
- [57] B. Zhang, S. Gu, B. Zhang, J. Bao, D. Chen, F. Wen, Y. Wang, and B. Guo, "Styleswin: Transformer-based gan for high-resolution image generation," in *CVPR*, 2022.
- [58] Y. Jiang, S. Chang, and Z. Wang, "Transgan: Two pure transformers can make one strong gan, and that can scale up," in *NeurIPS*, 2021.
- [59] J. Park and Y. Kim, "Styleformer: Transformer based generative adversarial networks with style vector," in *CVPR*, 2022.
- [60] "Dall-e mini," <https://github.com/borisdayma/dalle-mini>.
- [61] J. Betker, G. Goh, L. Jing, T. Brooks, J. Wang, L. Li, L. Ouyang, J. Zhuang, J. Lee, Y. Guo *et al.*, "Improving image generation with better captions," *Computer Science*. <https://cdn.openai.com/papers/dall-e-3.pdf>, vol. 2, no. 3, p. 8, 2023.
- [62] M. Heusel, H. Ramsauer, T. Unterthiner, B. Nessler, and S. Hochreiter, "Gans trained by a two time-scale update rule converge to a local nash equilibrium," *Advances in neural information processing systems*, vol. 30, 2017.
- [63] N. Martin and H. Maes, "Multivariate analysis," *London, UK: Academic*, 1979.
- [64] E. J. Hu, Y. Shen, P. Wallis, Z. Allen-Zhu, Y. Li, S. Wang, L. Wang, and W. Chen, "LoRA: Low-rank adaptation of large language models," in *International Conference on Learning Representations*, 2022.
- [65] J. Song, C. Meng, and S. Ermon, "Denoising diffusion implicit models," in *International Conference on Learning Representations*, 2021.

- [66] T. Karras, M. Aittala, T. Aila, and S. Laine, “Elucidating the design space of diffusion-based generative models,” *Advances in Neural Information Processing Systems*, vol. 35, pp. 26 565–26 577, 2022.



Tianyun Yang is currently pursuing her Ph.D. degree at the Institute of Computing Technology, Chinese Academy of Sciences, Beijing, China. She received her B.E. degree from Wuhan University in 2019. Her research interests lie in AI safety.



Juan Cao is a professor at the Institute of Computing Technology, Chinese Academy of Sciences, where she received her Ph.D. degree in 2008. Her research interests include multimedia content analysis and fake multimedia detection. She has over 90 publications in international journals and conferences including TKDE, TIP, KDD, WWW, CVPR, etc.



Danding Wang received her B.E. degree from Beihang University, China, in 2016. She received her Ph.D. degree from the National University of Singapore, Singapore, in 2021. She is currently an assistant researcher in the Media Synthesis and Forensics Lab of the Institute of Computing Technology, Chinese Academy of Sciences. Her research interests include explainable AI, misinformation detection, and AIGC detection.



Chang Xu is ARC Future Fellow and Associate Professor at the School of Computer Science, University of Sydney. He received the University of Sydney Vice-Chancellor’s Award for Outstanding Early Career Research. His research interests lie in machine learning algorithms and related applications in computer vision. He has published over 100 papers in prestigious journals and top-tier conferences.

APPENDIX

A. Attribution Robustness Analysis

Different Generation Configurations. In the generation phase, diffusion models offer various configurable parameters, such as the sampling step, sampling scheduler, guidance scale, and the resolution of the generated images. These variations in setup can influence the quality of the generated images. To assess whether the extracted fingerprint remains stable amidst these variations, we conducted evaluations on three Stable Diffusion models: SD1.5, SD2.1, and SDXL 1.0. We systematically varied these configurations during image generation. Samplers from DDIM [65], PNDM, LMS, and Euler [66] were used randomly. The guidance scale was uniformly sampled between 5 and 10, while image dimensions varied with widths and heights ranging from 256 to 1024 pixels, and sampling steps from 20 to 50. Figure 15 illustrates the t-SNE plots of fingerprint embeddings extracted by our fingerprint extractor (Only-Syn), from models under both fixed and varied generation configurations. The results demonstrate that images with varied generation settings exhibit fingerprints as stable as those with fixed settings, underscoring the robustness of our trained fingerprint extractor to variations in diffusion generation configurations.

Image Perturbations. Images generated by models may undergo various post-processings during transmission on social media. To evaluate the robustness of our fingerprint extractor (Only-Syn), we tested it against the two most common types of post-processing: JPEG compression and crop resizing. For these tests, we utilized 'ImageCompression' and 'RandomResizedCrop' from the Albumentations library, where 'RandomResizedCrop' randomly crops a patch from the image and resizes it back to the original dimensions. As depicted in Figure 16, we charted the model identification accuracy alongside the JPEG compression rate and crop ratio. It was observed that our trained fingerprint extractor is relatively robust to the crop resizing post-processing, yet exhibits sensitivity to JPEG compression. To mitigate this sensitivity, we incorporate them as a form of data augmentation during training. The immunized fingerprint extractor, as depicted by the red line in the results, demonstrates strong robustness against crop resizing and improvement in resilience against JPEG compression. However, the performance does not fully recover to that of the unaltered data under JPEG compression. This is primarily because JPEG compression can significantly alter the spectrum pattern, thereby degrading the original pattern left by the model, as also noted in [31]. Addressing the robustness against JPEG compression will be a focus of the future work.

B. Experimental Setups

When training on synthetic models, the real images used to generate fingerprinted images are firstly resized to 128×128 . The batch size is set to 200. The initial learning rate is $1e^{-4}$ with a warm up cosine scheduler. The margin for the triplet loss is 0.3. The total training epoch is 40.

C. Model Verification Cases

We provide some model verification cases produced by our model fingerprint extractor in Figure 17, Figure 18, and

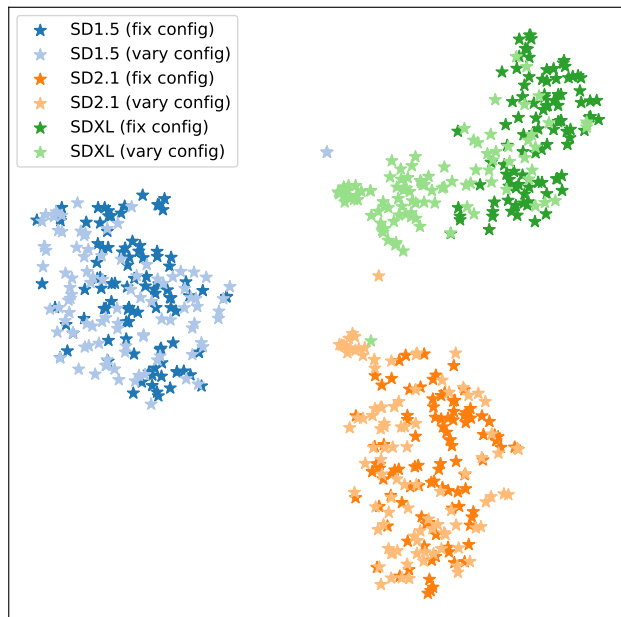


Fig. 15: t-SNE visualization of extracted fingerprints from diffusion images with fixed and varied generation configurations.

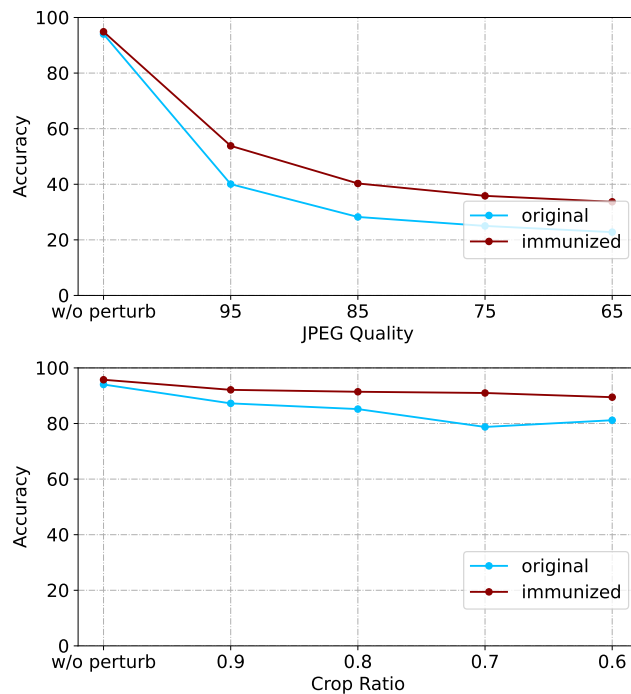


Fig. 16: Model identification accuracy of original and immunized fingerprint extractor under JPEG compression and crop resizing.

Figure 19. Model verification aims at verifying whether two generated images are from the same model by comparing extracted fingerprints. The threshold to make the prediction is empirically set as 0.81, which is the best threshold of model verification on the Text2Image models in Table I. *It is important to note that, to evaluate the zero-shot attribution ability in the open world, the fingerprint extractor producing these results is solely trained on synthetic models, without having seen any images from the real generative models tested below.*

D. Limitations

As depicted in Figure 14 in the main text, the extracted fingerprints from images of LoRA-equipped models are similar to their Base models, which allows us to attribute the LoRA variants to their base models. However, this also indicates a limitation of our method in distinguishing different LoRA variants from the same base model. We leave this more fine-grained model attribution challenge for future work.

Fingerprint Similarity: 0.7192
 Ground Truth: **Different Model**
 Prediction Result: **Different Model**

Dalle2



Image from the showcases on the Dalle-2 webpage. [Link](#)
 Prompt: An armchair in the shape of an avocado.

Dalle3



Generated by Dalle-3 in ChatGPT.
 Prompt: An armchair in the shape of an avocado.

Fingerprint Similarity: 0.7927
 Ground Truth: **Different Model**
 Prediction Result: **Different Model**

Dalle2



Image from the showcases on the Dalle-2 webpage. [Link](#)
 Prompt: "A sea otter with a pearl earring" by Johannes Vermeer.

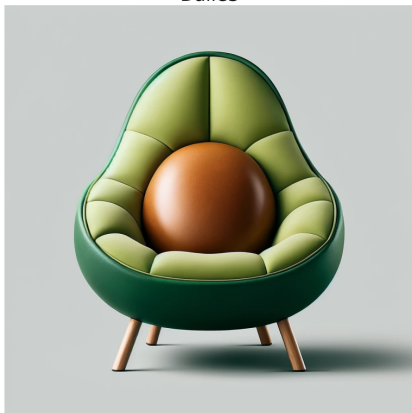
Dalle3



Generated by Dalle-3 in ChatGPT.
 Prompt: "A sea otter with a pearl earring" by Johannes Vermeer.

Fingerprint Similarity: 0.9045
 Ground Truth: **Same Model**
 Prediction Result: **Same Model**

Dalle3



Generated by Dalle-3 in ChatGPT.
 Prompt: An armchair in the shape of an avocado

Dalle3



Generated by Dalle-3 in ChatGPT.
 Prompt: "A sea otter with a pearl earring" by Johannes Vermeer

Fig. 17: Model verification results on images from Dalle-2 and Dalle-3.

Fingerprint Similarity: 0.7693
 Ground Truth: **Different Model**
 Prediction Result: **Different Model**

sd15



Prompt: Stark white appliances stand out against brown wooden cabinets.

sdxl



Prompt: Stark white appliances stand out against brown wooden cabinets.

Fingerprint Similarity: 0.6534
 Ground Truth: **Different Model**
 Prediction Result: **Different Model**

sd15



Prompt: Two apples, an orange, some grapes and peanuts.

sdxl



Prompt: Two apples, an orange, some grapes and peanuts.

Fingerprint Similarity: 0.9463
 Ground Truth: **Same Model**
 Prediction Result: **Same Model**

sdxl



Prompt: Two apples, an orange, some grapes and peanuts.

sdxl



Prompt: Stark white appliances stand out against brown wooden cabinets.

Fig. 18: Model verification results on images from Stable Diffusion models.

Fingerprint Similarity: 0.9314
Ground Truth: **Same Model**
Prediction Result: **Same Model**

RealCartoon-XL v2



Image from <https://civitai.com>.
Link

RealCartoon-XL v2



Image from <https://civitai.com>.
Link

Fingerprint Similarity: 0.9612
Ground Truth: **Same Model**
Prediction Result: **Same Model**

AniImagine XL V3.1



Image from <https://civitai.com>.
Link

AniImagine XL V3.1



Image from <https://civitai.com>.
Link

Fingerprint Similarity: 0.7779
Ground Truth: **Different Model**
Prediction Result: **Different Model**

RealCartoon-XL v2



Image from <https://civitai.com>.
Link

AniImagine XL V3.1



Image from <https://civitai.com>.
Link

Fig. 19: Model verification results on images from <https://civitai.com>.